Ion Implantation as an Approach for Structural Modifications and Functionalization of Ti 3 C 2 T x MXenes

Hanna Pazniak, Mohamed Benchakar, Thomas Bilyk, Andrea Liedl, Yan Busby, Céline Noël, Patrick Chartier, Simon Hurand, Marc Marteau, Laurent Houssiau, et al.

Ion Implantation as an Approach for Structural Modifications and Functionalization of $Ti_3C_2T_x$ MXenes

Hanna Pazniak,[,†] Mohamed Benchakar,[‡] Thomas Bilyk,[†] Andrea Liedl,[&] Yan Busby,[§] Céline Noël,[£] Patrick Chartier,[†] Simon Hurand,[†] Marc Marteau,[†] Laurent Houssiau,[/] Rosanna Larciprete,[#] Paolo Lacovig,[//] Daniel Lizzit,[//] Ezequiel Tosi,[//] Silvano Lizzit,[//] Jérôme Pacaud,[†] Stéphane Célérier,[‡] Vincent Mauchamp,[*,†] Marie-Laure David[*,†]*

[†]Institute Pprime, UPR 3346 CNRS, Université de Poitiers, ISAE-ENSMA, BP 30179, 86962 Futuroscope-Chasseneuil Cedex, France

[‡]Institut de Chimie des Milieux et Matériaux de Poitiers (IC2MP), Université de Poitiers, CNRS, F-86073 Poitiers, France

[&]INFN-LNF, P.O. box 13, 00044 Frascati (Rome), Italy

[§]Nanomatériaux pour les Systèmes Sous Sollicitations Extrêmes (NS3E), ISL-CNRS-UNISTRA UMR 3208, French-German Research Institute of Saint-Louis, 68301 Saint-Louis, France

[£]IMEC, Kapeldreef 75, B-3001 Heverlee, Belgium

[/]Namur Institute of Structured Matter (NISM), University of Namur, 5000 Namur, Belgium

[#]CNR-Institute for Complex Systems (ISC), 00185 Rome, Italy

[//]Elettra-Sincrotrone Trieste S.C.p.A., AREA Science Park, S.S. 14 km 163.5, 34149 Trieste, Italy

E-mails: H.P. hanna.pazniak@univ-poitiers.fr; V.M. vincent.mauchamp@univ-poitiers.fr; M.-L.D. mldavid@univ-poitiers.fr

ABSTRACT: MXenes are a young family of two-dimensional transition metals carbides, nitrides, and carbonitrides with highly controllable structure, composition, and surface chemistry to adjust for target applications. Here, we demonstrate the modifications of two-dimensional MXenes by low-energy ion implantation, leading to the incorporation of Mn ions in $Ti_3C_2T_x$ thin films. Damages and structural defects caused by the implantation process are characterized at different depths by XPS on Ti2p core-level spectra, ToF-SIMS and with electron energy loss spectroscopy analyses. Results show that the ion-induced alteration of the damage tolerant $Ti_3C_2T_x$ layer is due to defects formation in both Ti and C sites, thereby promoting the functionalization of these sites with oxygen groups. This work contributes to the inspiring approach of tailoring 2D MXenes structure and properties through doping and defects formation by low-energy ion implantation to expand their practical applications.

KEYWORDS: $Ti_3C_2T_x$ MXene, ion-implantation, defects, ToF-SIMS, XPS, TEM-EELS

MXenes, with structure $M_{n+1}X_nT_x$, where M stands for an early transition metal, X is C and/or N, T_x is a surface termination and n = 1, 2, or 3, are single or few-layered two-dimensional (2D) transition metals carbides and/or nitrides successfully synthesized in 2011.[1] Rapidly after their discovery, MXenes, were considered as promising materials in many applications such as energy

storage,[2] sensing,[3] catalysis,[4] and optoelectronics.[5] Thanks to the wide chemical and stoichiometrical variability of parent MAX phases, where the A-group precursor elements usually belong to group 13 and 14 of the periodic table,[6] MXenes can be easily adjusted to target applications. With these possibilities, the MXenes exhibit high electrical conductivity,[7] hydrophilicity,[8] excellent mechanical properties,[9] and technological flexibility.[10-12] Among the large variety of chemical compositions of MXenes that were experimentally[13] and theoretically[14] investigated, $Ti_3C_2T_x$ is the first and the most intensively studied due to well-established synthesis protocols providing high-quality and high yield 2D materials.[15]

To further extend MXenes applications, many attempts were made to modify their properties by applying different approaches and methods for surface chemistry engineering.[16] A number of reports were dedicated to effective etching protocols to modify the $Ti_3C_2T_x$ surface.[17-20] Depending on the etching route, the selective etching of the MAX phase with fluoride and/or chloride-containing acid solutions, introduced different amounts of surface anion groups (=O, –OH, –F, –Cl), affecting the electronic density of states and other functional properties. Beyond allowing for the surface design, the etching protocol has also been adjusted to introduce defects in the MX core of the MXene sheets.[21] Termination-engineering of $Ti_3C_2T_x$ was also achieved by thermal annealing in vacuum or in different gas media.[22-24] In particular, the surface composition and the electronic properties were controlled by the annealing temperature allowing for the de-functionalization of $Ti_3C_2T_x$.[24] Several studies demonstrated the successful surface functionalization of $Ti_3C_2T_x$ with carboxyl,[25] glycine groups,[26] and silane coupling agents,[27,28] resulting in the improvement of the $Ti_3C_2T_x$ stability[25,27] and the charge percolation, which allowed implementing the thin films in areas such as antibacterial coatings, fuel cells, surface-initiated polymerization, and absorbers.

Unfortunately, the multiple process variables such as the solution concentration, annealing temperature, etching duration, and media pH hinder the process reliability and reproducibility, resulting in a randomly distributed surface functionalization. The theory predicts that the bandgap and the magnetic properties could be engineered by adjusting the thin film chemistry and terminations.[29] However, the lack of experimental verification confirms the practical difficulty of such termination-engineering approach.

Introducing additional species into the layered MXene structure *via* ions intercalation is another strategy to control their properties.[30] MXenes can be intercalated both chemically and electrochemically by mono- and multivalent metal cations (such as H^+, Li^+, Na^+, K^+, Ca^{2+}, Mg^{2+}), as well as by organic molecules.[30-36] Cation-intercalated engineering allows controlling the interlayer distance, which is directly proportional to the hydration size of the intercalated species, and to tune the mechanical and actuation properties of Ti_3C_2 MXene.[35] This resulted in the enhancement of the capacitance[31,32,36] and sensing[34] properties. However, since ions intercalation mainly impacts the interlayer distance, it does not allow to deeply modify their physical properties.

One of the recent chemical-based approaches to modify MXenes properties is the so-called "targeted etching". It produces vacancy-ordered MXenes[37,38] derived from in-plane ordered MAX phase solid solutions by selectively etching both the *A*-element (Al) and the *d*-element on the *M*-position (for example Y or Sc). However, when the structure gets more complex, as for quarterly systems, a complete conversion of the MAX phase to a 2D structure becomes difficult.

Alternative strategies to tune MXenes properties include physical treatments with UV-ozone,[39] electron beam irradiation,[40] and plasma treatment.[41] Nevertheless, even if these approaches have shown some positive results, systematic and reproducible demonstrations are still missing.

Among the physical approaches used to infer specific characteristics to materials, ion-implantation has been widely used in the semiconductor industry as a powerful technique to modify the properties and structure of bulk materials through the controllable doping and damage formation.[42] Whereas this technology is very mature in the silicon-based electronic device manufacturing, exciting applications have emerged such as in the solid-state quantum bits domain.[43,44]

Recently, ion-implantation was extended to atomically-thin 2D materials,[45] such as graphene,[46-54] transition metals dichalcogenides (TMDs, mostly MoS_2[52,55] and WSe_2[56]) and hexagonal boron-nitride.[52] It was shown that low-energy ion implantation, with energy from several eV to tens of keV, causes structural changes on 2D materials, which considerably impact the properties of materials due to the substitution of target atoms by doping ions and/or by the introduction of defects. So, doping graphene with ~1% $^{11}B^+$ and $^{12}C^+$ ions induces a strong negative magnetoresistance at high magnetic field,[46] while doping with nitrogen ions effectively raises the position of the Fermi level thus affecting the graphene electronic properties. The incorporation of phosphorus ions in 2D TMDs enhances the photoluminescence, while in graphene it tunes the work function in a wide range (4.15-4.85 eV).[57] The defects created by the ion-implantation in 2D structures are a function of the implantation conditions and implanted ions species. At low fluence and energy below 100 eV, single vacancies,[45,54] Stone-Wales defects[45] and dangling bonds[54] are produced in single or few-layer 2D structures. At higher energy, structural disorder and amorphization are observed.[45] It was successfully demonstrated that defect engineering in graphene and 2D TMDs materials by ion-implantation allows tuning the electronic properties,[49] the morphology and the stoichiometry of materials. The latter leads to unusual properties such as the metallic-like behavior of non-stoichiometric MoS_2[54] and WSe_2.[56]

In this paper, we carry out a systematic modification of $Ti_3C_2T_x$ MXenes by ion-implantation with manganese ions. This was motivated by recent theoretical predictions on the tuning of MXenes' magnetic properties *via* strain, doping or defect engineering that attracted wide interest in the spintronics and quantum information communities.[58] We find, that ion-implantation leads to preferential Ti atoms sputtering with respect to the C atoms in the MXene layer. Such a sputtering offers new crystallographic sites available for the functionalization groups (oxygen) with a dramatic increase in the O content. The structural changes and damages introduced by the ion-implantation are investigated by spectroscopic studies, combining high resolution X-ray Photoelectron Spectroscopy (XPS) and Electron Energy-Loss Spectroscopy (EELS) in a Transmission Electron Microscope (TEM). The possibility of tuning the ion-implantation parameters in a wide range (nature and concentration of ion species, implantation energy) allows modifying and controlling the physical properties of MXenes.

RESULTS AND DISCUSSION

MXene film characterization

The $Ti_3C_2T_x$ MXenes were synthesized using MILD[59] (minimally intensive layer delamination) conditions as described in the *Materials and Methods* section. The schematic structure and a typical transmission electron microscope (TEM) micrograph of delaminated $Ti_3C_2T_x$ flakes obtained from a colloidal solution are shown in **Figure 1a-1b**. The flakes are irregular in shape with an average lateral size of 2–10 μm. The flakes surface shows no visible defects, holes, nor impurities of the oxidized phase. The Selected Area Electron Diffraction (SAED) of the $Ti_3C_2T_x$ flakes (**Figure 1b, inset**) shows the hexagonal arrangements originating from the parent Ti_3AlC_2 precursor symmetry. To carry out ion implantation, described in the next section, we fabricated

$Ti_3C_2T_x$ multi-layer films by spin-coating to achieve approximately a thickness of 100 nm. The Scanning Electron Microscopy (SEM) image of the fabricated film (**Figure 1c**) shows that the Si/SiO_2 substrate is fully and homogeneously covered since there are no naked regions over a considerably large area. The cross-section SEM image (**Figure 1c inset**) reveals a compact film structure with well-resolved stacked layers aligned parallel to the Si/SiO_2 substrate. The average film thickness is about 100 nm with ~20 nm surface roughness associated with the spin-coating processing. The comparison between the X-Ray Diffraction (XRD) patterns of the as-prepared $Ti_3C_2T_x$ powder and thin film (Figure 1d) shows that the film is characterized only by the sharp and intense low angle (002) peak and the disappearance of the (110) peak confirming that film is well-aligned along the *c*-direction with the derived *c*-lattice parameter of 29.8 Å.

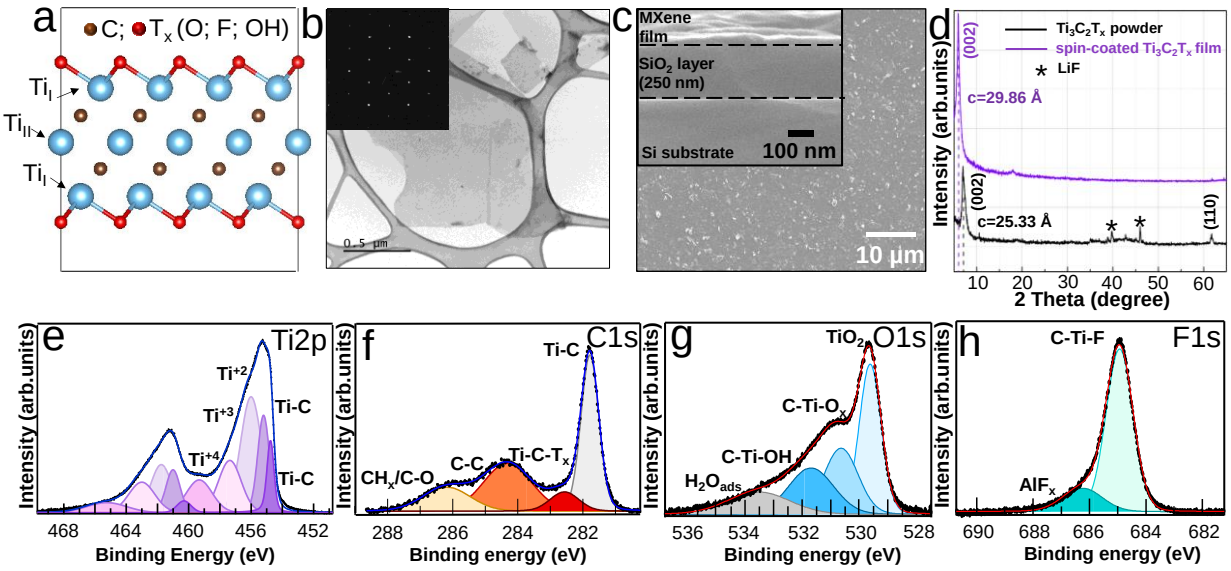

Figure 1. MXenes powder and thin film characterization. a) The schematic structure[60] of monolayer $Ti_3C_2T_x$ MXene; Ti_I and Ti_{II} are surface and core Ti atoms, respectively, T is a surface functional group; b) TEM micrograph of $Ti_3C_2T_x$ flakes obtained from a delaminated colloidal MXene solution with corresponding SAED pattern (inset); c) SEM image of MXene spin-coated thin film with a corresponding cross-section (inset) taken in Secondary Electron Imaging (SEI)

mode; d) XRD patterns of the as-synthesized $Ti_3C_2T_x$ powder and spin-coated thin film; e), f), g), h) High-Resolution (HR) core-level spectra of Ti2p, C1s, O1s, and F1s from a spin-coated MXene film.

The HR-XPS spectra from the freshly deposited $Ti_3C_2T_x$ thin film are shown in Figures 1e-1h. For the Ti2p spectrum the main doublets related to the MXene structure have the 3/2 spin orbit component at 454.8, 455.2, 456.0, 457.4 eV,[61] whereas the minor peak, appearing at 459.3 eV (Ti^{+4}) is attributed to the formation of a small amount of oxidized TiO_2 phase. Both Ti2p peaks at 454.8 and 455.2 eV are attributed to Ti-C bonds in the MXene structure, being the peak at higher binding energy related to the presence of neighboring lattice defects.[61]

The peaks located at 456.0 and 457.4 eV are attributed to Ti^{+2} and Ti^{+3} and correspond to titanium atoms bonded with carbon and functional groups C–Ti–O, C–Ti–F,[20] and C–Ti–OH.[61] For the C1s spectrum, the main peak, related to the Ti–C bonds appears at 281.8 eV and the second one attributed to Ti–C–T_x appears at higher energy (282.5 eV). The two minor peaks, at 284.3 and 286.2 eV are assigned to graphitic C–C bonds and organic CH_x/C–O contaminations. The O1s spectrum shows three peaks at 529.6, 530.7, and 531.7 eV attributed to the functionalized C–Ti–O_x and C–Ti–OH phases, respectively.[62] The fourth minor component at 533.4 eV is related to adsorbed H_2O. The F1s spectrum shows a strong component at 685.0 eV attributed to the C–Ti–F_x bonds arising from the MXene surface functionalized by fluorine groups and a weak shoulder fingerprint of AlF_x at 686.3 eV.[61]

Ion implantation of $Ti_3C_2T_x$ thin films

The 100 nm-thick $Ti_3C_2T_x$ films were directly exposed to the ion beam as detailed in *Materials and Methods*. For many 2D materials such as MoS_2[63] or graphene, because of growing limitations, ion implantation was performed only up to few-layered structures. In order to reduce the structural

damages, the doping of few-layers 2D materials was performed at low beam energy (25 eV – 2 keV) or by depositing an additional protection layer[57,64] on the top of the 2D material. In our case, the 100 nm thick multi-layer MXenes film allows using a higher energy beam (tens of keV) to implant the whole film with Mn ions. The $^{55}Mn^{+}$ implantation is performed at 60 keV at fluences of $1 \cdot 10^{15}$ and $1 \cdot 10^{16}$ ions/cm^2 to generate specific ion distribution/damage profiles with projectile depths compatible with the thickness of the MXene film, according to Stopping and Range of Ions in Matter (SRIM) simulations shown in Figure 2a.

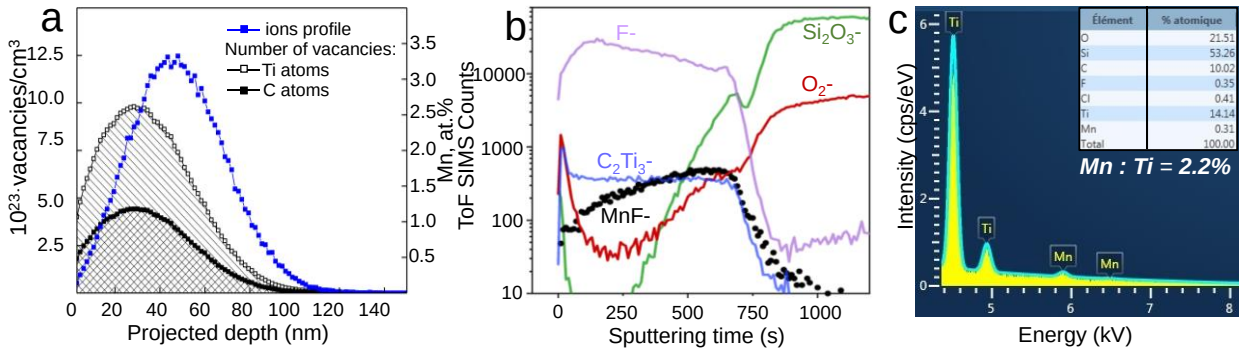

Figure 2. (a) The SRIM simulated depth profiles of Ti and C atoms vacancies (black curves) and $^{55}Mn^{+}$ ion distribution (blue curve) within the $Ti_3C_2T_x$ thin film following the ion-implantation with $1 \cdot 10^{16}$ ions/cm^2 fluence at 60 keV energy. The Ti and C vacancy profiles are given for a qualitative estimation; (b) ToF-SIMS depth profiles of $^{55}Mn^{+}$-implanted $Ti_3C_2T_x$ thin films at 60 keV with $1 \cdot 10^{16}$ ions/cm^2 fluence; (c) EDS spectrum of $Ti_3C_2T_x$ thin film implanted with $1 \cdot 10^{16}$ Mn-ions/cm^2 at 60 keV.

Based on SRIM calculations, for 60 keV energy of Mn^{+} ions, the projected range and the average straggling are equal to 47.7 and 20.3 nm respectively. Thus, the Mn-ions distribution is Gaussian-like and the maximum should occur in the middle of the $Ti_3C_2T_x$ film (Figure 2a). The simulated damage profile (numbers of vacancies on Ti and C atoms) is more asymmetric than ions profile and reveals that the near-surface region of the film might be highly damaged. The tail of the

damage distribution is observed close to the Si/SiO_2 substrate which means that in this region the film should be less damaged. Moreover, the SRIM calculations gives the value of the sputtering yield, Y, defined as an average number of atoms leaving the surface of a solid per incident particle. The sputtering yield of Ti atoms from the simulated structure of Ti_3C_2 is 0.22 atoms/ion, whereas the sputtering yield of C atoms is 0.07 atoms/ions. Since the SRIM code applies to bulk materials, as an approach to simulate the implantation profile, we have considered the Ti_3C_2 density of 3.20 g/cm^3 as the average density of the multilayer stacked thin film, which might be overestimated. Thus, we account for the SRIM results only from a qualitative point of view, suggesting the preferential sputtering of Ti atoms as compared with C atoms during Mn implantation.

It is difficult to directly translate SRIM results to the real ion distribution in the MXenes film since bulk materials with homogeneous density and exact chemistry are sensibly different from atomically-thin single- and multilayer stacked 2D materials. To obtain experimental evidence of the Mn profile in the $Ti_3C_2T_x$ film and correlate these results with SRIM calculations, we performed Time-of-Flight Secondary Ion Mass-Spectroscopy (ToF-SIMS) (Figure 2b) on ion-implanted films. The implanted samples were sputtered with low-energy (0.5 keV) Cs^+ beam and analyzed with a short impulse of Bi_3^+ beam at 25 keV. Cesium sputtering was chosen because it is a universal sputtering source for organic and inorganic materials which does not introduce major artifacts (no preferential sputtering or reduction of metals nor accumulation of in depth-modifications) and will not significantly modify the chemical composition of the exposed sample surface. The ToF-SIMS depth profile analysis clearly shows that the Mn distribution, assessed by the MnF^- ion, is uniform in the *log* plane and it increases monotonically along with the depth (sputtering time) of the Ti_3C_2 film which shows a stable intensity as monitored by the $C_2Ti_3^-$ ion. We selected the MnF^- ions signals because of its strong intensity and the absence of mass overlaps

with other ions. The maximum of the Mn concentration is found close to the SiO_2 substrate which is identified by the rise of $Si_2O_3^-$ and O_2^- signals. We also observe a raise of the $Si_2O_3^-$ signal at the beginning of the profile which is a frequently observed feature ascribed to surface contamination by polydimethylsiloxane. The discrepancy between the ToF-SIMS and SRIM profiles is possibly explained by (*i*) the 2D nature of Van der Waals bonding between MXene sheets, (*ii*) the roughness of the film or (*iii*) the Cs^+ sputtering-related artifacts.[65,66] Despite this, the experiment confirms that the Mn doping is successfully achieved in the fabricated thin film as proved by the bulk-sensitive Energy-dispersive X-ray Spectroscopy (EDS) analysis (Figures 2c), indicating ~2.2 at.% Mn doping which is lower as compared with the value at the maximum of the SRIM profile.

Spectroscopic characterization of implanted $Ti_3C_2T_x$ thin films

To follow the structural damages and chemical modifications induced in the $Ti_3C_2T_x$ film surface by the Mn-ions implantation we perform high-resolution XPS depth profiling (Figure 3) and EELS analysis (Figures 4-5).

In the former case the sample was sputtered with low-energy (500 eV) Ar^+ beam which, as well as Cs sputtering in ToF-SIMS, allows limiting in-depth damages for 2, 7, 12 and 22 min and the Ti2p spectra measured at increasing depths are shown in Figure 3a together with the results of the best-fitting analysis. In agreement with Figure 1e, four spectral components are identified, labeled as Ti–C (from the MXene structure at ~455.2 eV binding energy), Ti^{+2}, Ti^{+3} and Ti^{+4} (from oxidized TiO_2 phase, at ~459.5 eV). After implantation, the Ti2p spectrum looks very different from the pristine film (Figure 1e); we observe a very intense contribution from the oxide phase, in particular, the Ti^{+4} doublet which dominates the spectrum. After 22 min of Ar^+ sputtering, the oxidized layer is partially removed and the Ti2p spectrum is peaked at ~ 455.5 eV and starts to resemble that of freshly deposited $Ti_3C_2T_x$ film (see **Figure 1e**). The rather long sputtering time required to partially

decrease the oxidized phase testifies that the chemical modification induced by the implantation extends well below the film surface (7-8 nm from the surface).

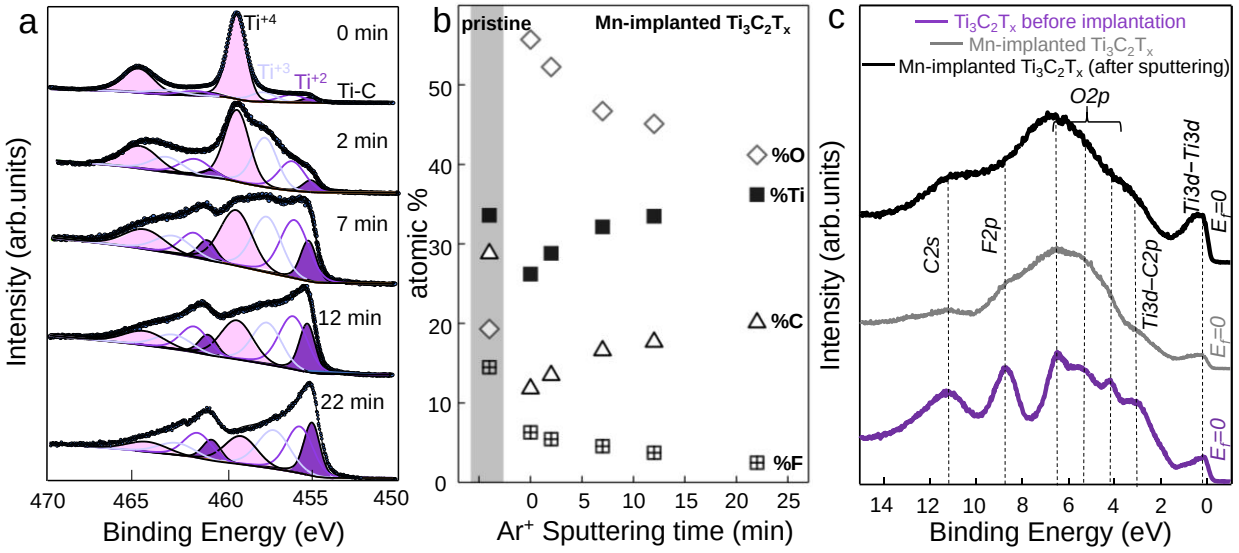

Figure 3. a) Ti2p HR-XPS spectra of Mn^+-implanted $Ti_3C_2T_x$ thin film ($1 \cdot 10^{15}$ ions/cm^2 at 60 keV) after sputtering at different times; b) Evolution of the film composition (O, Ti, C, and F atomic %) with the sputtering time (500 eV Ar^+) as derived from the analysis of survey spectra for the Mn-implanted film as compared to the pristine $Ti_3C_2T_x$ film (before implantation); c) Valence band XPS spectra of pristine $Ti_3C_2T_x$ thin film, after implantation with $1 \cdot 10^{15}$ ions/cm^2 at 60 keV, and after 22 min Ar^+ ion beam etching.

However, the XPS measurements point out that both the $Ti_3C_2T_x$ film chemical composition in the surface and its depth are modified by the Mn-ions implantation; in particular, the oxygen content (Figure 3b) and Ti^{3+} component are still higher as compared to the pristine film (Figure 1e). This suggests that the Ti–C bonds dissociated by the impinging Mn-ions quickly react with oxidizing species present in the background pressure inside the implanter or, more effectively, with atmospheric water and oxygen adsorbates when the reactive $Ti_3C_2T_x$ surface is extracted from the implanter. The formation of an oxidized phase on the top of the implanted surface was also

observed after ion-irradiation of 2D MoS_2 with swift heavy ions resulting in production of active low-coordinated Mo atoms.[67,68] The observed increase in the Ti-O_x and Ti-OH bonds (Ti^{3+} component) more in depth agrees with the decaying O_2^- profile in the ToF-SIMS measurements during the 300 s of Cs^+ sputtering (Figure 2b) which is well above the time necessary to typically remove oxidized surface contaminating layers (*i.e.* few seconds).

From the survey XPS spectra measured at 1030 eV (Supporting Information, Figure S1) we have calculated the sample composition as a function of the sputtering time (Figure 3b). The slight higher amount of C found in pristine MXene film as compared with stoichiometric value is ascribed to the surface contamination. From the evolution of the chemical composition with the Ar^+ sputtering time, we can follow the non-stoichiometric ratio between Ti and C atoms. Namely, while both %Ti and %C increase with the sputtering time (t), the Ti/C ratio decreases from 2.1 (t=0 min) to 1.8 (t=22 min) thus slowly approaching the nominal value of 1.5 (Ti_3C_2). Simultaneously, the fluorine and oxygen content decreases. However, even after t=22 min, the amount of oxygen is still two times higher than in the pristine film, indicating that defective sites are still occupied by oxygen atoms mainly forming Ti^{+3} state.

From the valence band of $Ti_3C_2T_x$ films (**Figure 3c**) we immediately see that the electronic structure is modified by ion implantation; the main Ti3d-C2p, O2p, and F2p[69] bands are strongly broadened and can hardly be resolved after Mn-ion implantation and after Ar^+ ion beam sputtering. This indicates a structural disorder in the Mn-implanted MXene structure. Nevertheless, the valence band maximum is still at the Fermi level (E_f), confirming that the implanted MXene film is still metallic with Ti3d states at E_f. We conclude that, despite the structural damages due to the $1 \cdot 10^{15}$ Mn/cm^2 implantation and induced increase of O content, the MXene maintains its metallic character.

Next, TEM-EELS are performed to better understand damages induced by ion-implantation. Electron spectroscopy has been demonstrated as powerful tool for the investigation of radiation-induced damages at the local scale in various materials including MAX phases and graphite.[70,71] The changes in the fine structure or an energy shift is an indication of different chemical compositions and/or crystallographic structure modification.[72]

In order to get a complementary picture of the films, especially the region with the higher Mn amount, TEM-EELS has been performed on very thick parts extracted from the two spin-coated films implanted at $1 \cdot 10^{15}$ and $1 \cdot 10^{16}$ ions/cm². The thicknesses of the two regions were similar and correspond to the thickness to inelastic mean free path ratio of 0.65 to 0.7. (Figure 4).

By recording EEL spectra at the Mn-$L_{2,3}$ edges in the implanted films (Figure 4a), we observed that the sample implanted at $1 \cdot 10^{15}$ ions/cm^2 shows almost negligible Mn-L_3 line; this very low doping reasonably agrees with SRIM calculations predicting the Mn concentration of ~0.32 at.% (Supporting Information, Figure S2). On the other hand, a more defined and sharper Mn-L_3 line is obtained when the implantation fluence is raised to $1 \cdot 10^{16}$ ions/cm^2. However, the intensities of Mn-$L_{2,3}$ lines of $Ti_3C_2T_x$ films at both fluences are weak and detailed information about the Mn chemical environment difficult to extract. The F-K edge signal in the investigated zones is rather low as compared with pristine un-implanted film (Figure 4a, inset).

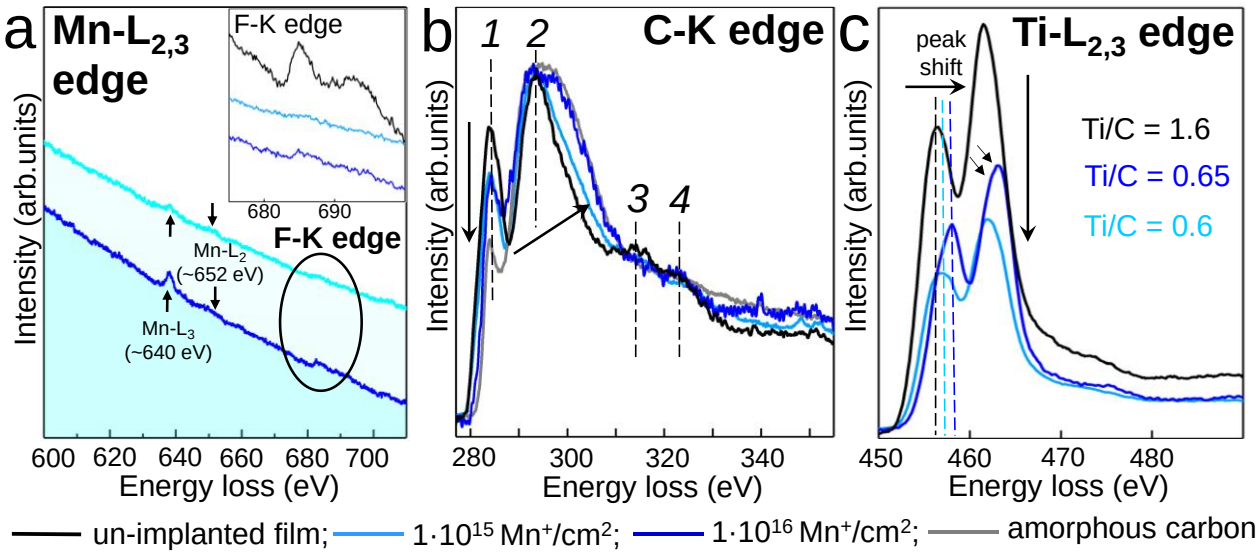

Figure 4. Mn-$L_{2,3}$ (a), C-K (b), and Ti-$L_{2,3}$ edges (c) EEL spectra of $Ti_3C_2T_x$ films before and after Mn-implantation at 60 keV with $1\cdot10^{15}$ and $1\cdot10^{16}$ ions/cm^2 fluence. C-K edge EELS spectrum of amorphous carbon is recorded as the reference.

In order to characterize the Ti-C bonding of the $Ti_3C_2T_x$ structure after implantation at $1\cdot10^{15}$ and $1\cdot10^{16}$ ions/cm^2 fluences, we compare the EEL spectra at C-K and Ti-$L_{2,3}$ edges in implanted and un-implanted films (Figure 4b-4c). Amorphous carbon is also recorded for reference. The C-K edge EELS signal from pristine $Ti_3C_2T_x$ film shows the presence of four peaks which are typical for $Ti_3C_2T_x$ structure.[73] These peaks are still intense and well-resolved after implantation, however, according to the fluence, we observe a progressive decrease of peak 1 and a broadening of peaks 2, 3, and 4. In agreement with the lower fluence, the broadening of peak 2 in the C-K edge EELS spectrum for the sample implanted with $1\cdot10^{15}$ ions/cm² is lower than that for the $1\cdot10^{16}$ ions/cm² sample. The broadening testifies a higher structural disorder, which has been commonly observed in carbon-based materials when structural distortions take place.[71] These results confirm the fluence-dependent structural distortion in Ti–C layers after implantation and reveals that the amount of damage is being controllable over one or two orders of magnitude by tuning the fluence.

Very important, neither for the $1 \cdot 10^{15}$ nor $1 \cdot 10^{16}$ ions/cm^2 fluences the structural disorder leads to the amorphization of the MXene as testified by SAED patterns given in **Figure S3** where no amorphization ring is observed. Under implantation conditions, the MXene flakes are thus damage tolerant allowing to use ion implantation to induce structural modification.

By normalizing spectra at the C-K edge, we can visualize the induced modifications at the Ti-L edge (Figure 4c). In particular, the drop in the intensity of the Ti-$L_{2,3}$ double peak (at 456 and 462 eV) indicates preferential sputtering of Ti atoms with respect to carbon atoms. The presence of titanium surface atoms (Ti_I) exhibiting smaller bounding energy than the bulk ones (Ti_{II}) in $Ti_3C_2T_x$ structure (Figure 1a) and the larger cross section of Ti atoms for elastic collisions involving Mn-ions as compared with C atoms dictates that defect production involving Ti atoms are statistically more probable.

Moreover, the energy shift of the Ti-$L_{2,3}$ lines (+0.6 and +1.6 eV depending on the fluence) indicates the progressive increase of Ti oxidation state[72] (Figure 3a). Having a closer look at the Ti-$L_{2,3}$ edge EELS spectrum for the sample implanted with $1 \cdot 10^{16}$ ions/cm², we notice that the lines are slightly asymmetric. However, the Ti-$L_{2,3}$ edge is clearly different from highly oxidized $Ti_3C_2T_x$ MXene where the asymmetry of four peaks is well-resolved (Supporting Information, Figure S4). The diffraction spots corresponding to tetragonal anatase phase of TiO_2 presented in SAED patterns of implanted MXenes (Supporting Information, Figure S3) originate from the oxidation of the top surface film layers. Since the EELS signal integrates information from the whole film thickness, the signal from distorted surface layers characterized by stronger oxidation is superimposed to the one from the underlying preserved film. Overall, the analysis of C-K and Ti-$L_{2,3}$ edges points out that ion-implantation induced damages on both C and Ti atoms without significant amorphization or phase transformation.

Based on the spectroscopic study provided on the implanted $Ti_3C_2T_x$ thick films we can conclude that ion implantation results in successful Mn incorporation with partial damaging of the $Ti_3C_2T_x$ crystal structure. The last is confirmed by the gradual drop of (002) peak intensity in XRD patterns (Supporting Information, Figure S5). The additional peaks on the implanted sample in Figure S5 are due to the SiO_2 substrate. This confirms the sputtering of Ti and C atoms in the near-surface layers induced by the ion-implantation.

Since the Mn concentration is negligible when the fluence of $1 \cdot 10^{15}$ ions/cm^2 is used, we further explored film implanted with $1 \cdot 10^{16}$ ions/cm^2. To get precise information about damages occurring in MXenes flakes upon implantation excluding surface oxidation effect, we detached the film from the substrate, put different parts of the film in ultra-high purity water and drop it on carbon-supported membrane. We analyze only buried sheets with EELS picking the signals from three different regions (R1-R3) (see Supporting Information, Figure S6, for detailed description), each of which may be related to a different implantation depth. The ratio between the film thickness and the inelastic mean free path (1/lambda) in R1, R2, and R3 are 0.40, 0.20 and 0.21 respectively, meaning that we analyze regions with different thicknesses. The results are shown in Figure 5 and corresponding SAED patterns of studied regions are in Supporting Information, Figure S7.

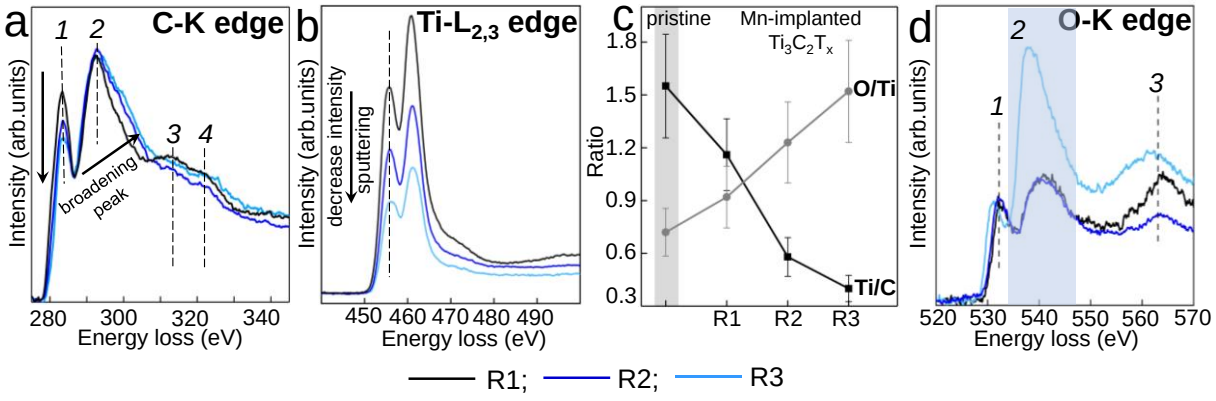

Figure 5. C-K (a), Ti-$L_{2,3}$ (b), and O-K (d) edges EEL spectra of different regions from $Ti_3C_2T_x$ films after Mn-implantation at 60 keV with $1 \cdot 10^{16}$ ions/cm^2. The O-K edge spectra were normalized on the first peak intensity. The Ti-$L_{2,3}$ edges are normalized to the C-K edge in (a). (c) The Ti/C and O/Ti composition ratio of different regions of Mn-implanted $Ti_3C_2T_x$ film as derived from elemental quantification of EELS spectra as compared to the pristine $Ti_3C_2T_x$ film (before implantation).

With respect to the pristine film spectrum, the C-K edge region (Figure 5a) features different degrees of distortions, going from barely almost un-modified peaks (in R1) to the 20-25% reduction of the peak 1 and comparable broadening of peak 2 (in R2 and R3). It is worth noticing that the peak 2 broadening is considerably lower respect to the one recorded in amorphous carbon (Figure 4a), evidencing a high damage tolerance of the Ti_3C_2 layer. According to the modeled SRIM profile, the less damaged structure should be in the middle of the film and close to the substrate.

From the Ti-$L_{2,3}$ edge spectra analysis we conclude that the R3 region, showing the highest broadening of C-K edge, is also the one showing the strongest drop of the Ti-$L_{2,3}$ peaks intensities (Figure 5b) and maximum sputtering yield of Ti atoms with respect to C atoms. The Ti content with respect to C is significantly reduced as compared to the pristine sample (Figure 5c). However, both damaged regions R2 and R3 do not show any shifting of the position of the peaks (Figure 5b) nor the presence of additional phases in SAED (Figure S7), confirming that oxidation is limited only to the more exposed top-surface sheets.

By analyzing the O-K edge (Figure 5d), we observe that EELS signal from implanted $Ti_3C_2T_x$ regions R1 and R2 shows the presence of three peaks similar to O-K edge usually observed in Ti_3C_2.[73] The O content (O/Ti) is gradually increased from R1 to R3 and correlates with Ti

sputtering (Ti/C) as evidence by EELS quantifications (Figure 5c). The R3 region, showing the maximum sputtering yield of Ti atoms, is also the one showing the highest O content. As can been seen, the O/Ti ratio in R3 region is about 1.5 and this value is twice that of the pristine un-implanted sample. This finding evidences the fact that Ti sputtering promotes new crystallographic sites, occupied by O atoms. This result is further confirmed by a strong modification of the O-K edge fine structure with a much more intense peak 2 (at ~ 538 eV) as compared with R1 and R2 regions indicating considerable changes in the local environment of the oxygen atoms (Figure 5d). A similar O-K edge EELS signal was experimentally recorded at graphene oxide.[74] This suggests that the extended zones of the MXene sheets surfaces where Ti has been preferentially sputtered offer new cites for oxygen bonding with the carbon planes, leading to a significant amount of oxygen atoms experiencing a G-O-like environment. This is in agreement with the SAED collected on region R3 (see Figure S7c) where additional rings, consistent with the GO structure, are also observed. These results are in agreement with Ti_3C_2 oxidation experiments reported recently and showing that Ti-vacancies promote the nucleation and oxidation of amorphous carbon clusters.[75] Moreover, *ab initio* molecular dynamics simulations[21] have shown that water molecules and oxygen adsorbates are preferentially located close to Ti vacancies. It could thus result in the formation of the graphene oxide structure at the local level as experimentally evidenced by TEM and EELS (Figure 5d, Figure S7c). The presence of peak 1 (Figure 5d), not ascribed to C-O like bonding, confirms that some of the original oxygen sites are preserved while the new ones are promoted. We can safely exclude that this feature is related to the formation of titanium dioxide in the sub-surface layers since the O-K edge spectrum of oxidized $Ti_3C_2T_x$ looks completely different from the one from the R3 region (see Supporting Information, Figure S4).

As a major result, thanks to the damage tolerance of the Ti_3C_2 sheets to ion implantation, this approach can be used to generate a high amount of both Ti and C extended defects, promoting oxygen functionalization as shown here using XPS and TEM-EELS. We conclude that the disordered character of the $Ti_3C_2T_x$ induced by ion-implantation is extremely favorable for the spontaneous functionalization of defective titanium and carbon sites with oxygen.

CONCLUSIONS

In this work we investigate ion-implantation of $Ti_3C_2T_x$ MXene thin films. The presence of Mn ions implanted at 60 keV was confirmed by ToF-SIMS depth profiling, EDS, and EELS analyses. Interestingly, the ion-implantation introduces a Mn doping profile and complex structural changes in stacked 2D MXenes while keeping their metal-like behavior. The XPS analysis evidenced that ion-implantation causes oxidation of the top-surface sheets due to the harsh sputtering of titanium and carbon atoms resulting in the formation of a large number of dangling bonds and reactive surface defects. The EELS proved the structural distortion gradient decay through the depth of $Ti_3C_2T_x$ film characterized by different degrees of defects formation in both Ti and C sites while keeping the original MXene structure suggesting their damage tolerance to ion-implantation.

The disorder induced in ion-implanted $Ti_3C_2T_x$ is found to be extremely favorable for the functionalization of defective titanium and carbon with oxygen functional groups, thereby increasing the amount of oxygen in MXene flakes and modifying their electronic structure. We believe this strategy is perspective and could be extended to other MXenes since oxygen functionalization is predicted to tune a band gap in different MXenes chemistry.

Since defects have been widely demonstrated to effectively tailor the carrier types and optical response in many 2D materials, ion implantation appears a practical, controllable and easily-

implementable tool to modify the electronic properties of MXenes. Defects are also beneficial for a number of applications such as photocatalysis, catalysis, micro-wave absorption and pseudocapacitance. The ion-implantation approach offers a great variety of adjusting parameters such as the dopant type, fluence and energy which can be selected to meet specific applications of MXenes in a wide range of research fields.

EXPERIMENTAL SECTION

MXenes synthesis and thin film preparation. The $Ti_3C_2T_x$ MXenes were synthesized from Ti_3AlC_2 precursor using the MILD (minimally intensive layer delamination) conditions, which means exfoliation of 0.5 g of Ti_3AlC_2 (initial particles sizes < 25 µm) at 40 °C in 10 ml solution of 0.8 g LiF dissolved in 9M HCl under continuous magnetic stirring during 24 h. The suspension obtained after etching, including $Ti_3C_2T_x$ and non-reacted Ti_3AlC_2, was centrifuged 8 times at 6000 rpm for 6 min and the supernatant liquid was systematically removed. The black $Ti_3C_2T_x$ slurry was then carefully collected and separated from the surface of the sediment $Ti_3C_2T_x/Ti_3AlC_2$ with a spatula. The slurry was then filtered, washed and dried one night under air at room temperature and finally stored under inert atmosphere. This synthesis method is partly based on the work of Alhabeb *et al.*[15]

The $Ti_3C_2T_x$ thin films were produced by spin coating of delaminated concentrated $Ti_3C_2T_x$ colloidal solution (concentration is ~ 70 mg/ml), obtained by simply manual shaking of a water suspension of multilayer MXenes as produced above, onto a Si substrate with 250-nm-thick SiO_2 (1x1) cm^2 area. Before deposition, the substrates were cleaned by sonicating in acetone in an ultrasonic bath, rinsing with isopropyl alcohol, and drying with compressed nitrogen. Thin films

were deposited using Polos SPIN150i/200i spin coater at room temperature in a multistep regime to achieve 100 nm thickness and dried overnight under vacuum conditions.

Ion-implantation. We prepared eight spin-coated $Ti_3C_2T_x$ films for one implantation since we used destructive techniques to characterize samples after implantation (XPS depth profile and ToF-SIMS). All samples were mounted on a cooled sample holder and directly exposed to the ion beam having an implantation surface of about 25 cm^2. Thin films were prepared before implantation to avoid contamination problems. $^{55}Mn^+$ ions of $1 \cdot 10^{15}$ and $1 \cdot 10^{16}$ ions/cm^2 were accelerated at 60 keV with probe currents of 2.1-7.0 μA and a chamber pressure of $\sim 5 \times 10^{-7}$ mbar at room temperature. The projectile trajectory of implanted ions was perpendicular to the surface of thin films. The damage and ion distribution depth profiles of $Ti_3C_2T_x$ thin film (density of 3.20 g/cm^3) were simulated using the Stopping and Range of Ions in Matter (SRIM) code.[76] The displacement energies used were E_d = 25 eV for Ti and E_d = 28 eV for C. The number of created vacancies were calculated using the detailed calculation with full damage cascades method.

$Ti_3C_2T_x$ thin film characterization. The X-Ray diffraction (XRD) patterns of the $Ti_3C_2T_x$ powder, spin-coated $Ti_3C_2T_x$ thin films before and after ion-implantation were collected at room temperature using D8 Diffractometer (Bruker Ltd. Germany) with a continuous θ–2θ scan with 0.017 ° 2θ/sec and Cu-Kα radiation (1.5406 Å) at U = 40 kV, I = 40 mA. Thin films' morphology and chemical composition were studied using JSM-7001F TTLS field emission gun scanning electron microscope (Jeol Ltd., Japan) equipped with an Energy Dispersive X-ray Spectrometer (EDS) from Oxford Instruments (UK).

The TEM samples were prepared by detaching the $Ti_3C_2T_x$ implanted film from the substrate by lightly brushing with a soft sharpened stick, put different fragments of the film in ultra-high purity water to avoid further agglomeration and drop it on Cu grid covered with a lacey carbon film. The

MXene films of different thicknesses were probed with the electron beam normal to the film. The Electron Energy Loss Spectroscopy (EELS) spectra were recorded in image mode in a JEOL 2200 FS microscope equipped with an in-column omega filter and operated at 200 kV. The energy resolution determined from the zero-loss peak full width at half maximum was 1.0 eV. The zero-loss peak was used to align in the energy scale the signal of the C-K edge, Ti-$L_{2,3}$ edge, and O-K edge spectra. The core edges were extracted from the background signal using a power law and were deconvolved from multiple scattering using the Fourier-ratio method. The acquisition conditions were optimized for each edge to avoid irradiation damages.

High-resolution (HR) core-level photoemission spectroscopy (XPS) was performed at the *SuperESCA* beamline of the Elettra synchrotron radiation facility (Trieste, Italy). Survey and HR core-level and valence band spectra of $Ti_3C_2T_x$ thin films were collected at a photon energy of 1030 eV and 100 eV respectively. For each spectrum, the binding energy was calibrated by measuring the Fermi level of the gold foil in contact with the sample. Core levels spectra were best-fitted with Voigt functions after Shirley background subtraction. The implanted MXenes thin films were repeatedly sputtered with 0.5 keV Ar^+ at $5 \cdot 10^{-6}$ mbar with the ion beam hitting the sample at 20 ° to normal. After each sputtering cycle survey and HR Ti 2p spectra were recorded at photon energy of 1030 eV.

Time-of-Flight Secondary Ion Mass-Spectroscopy (ToF-SIMS) depth profiles were acquired using a dual-beam ToF-SIMS IV spectrometer from ION-TOF GmbH (Münster, Germany) in non-interlaced mode, alternating 1-frame analysis with Bi^{3+} (energy 25 keV at the ion current of ~0.2 pA, analysis area of 100×100 μm^2) and 10 s of sputtering with 500 eV Cs^+ (at an ion current of ~25 nA, raster area of 250×250 μm^2) with a 1 s pause between cycles. When the erosion gun was

on, the sample surface was flooded using a defocused low-energy electron beam to sustain surface charge compensation.

ASSOCIATED CONTENT

Supporting Information. The Supporting Information is available free of charge on the ACS Publications website. Additional information about the survey spectra of $Ti_3C_2T_x$ film, SRIM simulated profile of implanted film, XRD patterns, TEM micrographs, and SAED patterns of implanted $Ti_3C_2T_x$ films, Ti-$L_{2,3}$ (b), and O-K edge EEL spectra of oxidized $Ti_3C_2T_x$ flakes, and schematic description of $Ti_3C_2T_x$ ion implantation procedure and the implanted film "structure".

AUTHOR INFORMATION

Corresponding Authors

*Emails: hanna.pazniak@univ-poitiers.fr (H.P.); vincent.mauchamp@univ-poitiers.fr (V.M.); mldavid@univ-poitiers.fr (M.-L.D.)

Notes

The authors declare no competing financial interest.

ACKNOWLEDGMENT

This work was partially funded by the "Région Nouvelle-Aquitaine" and the European Regional Development Fund (ERDF 2014-2020) within the NanoTrans project No. PC-2016-2916910. H.P. and R.L. thanks the Elettra Synchrotron Facility (proposal №20190484). The research leading to this result has been supported by the project CALIPSOplus under Grant Agreement 730872 from the EU Framework Programme for Research and Innovation HORIZON 2020. The authors also

acknowledge financial support from the French research ministry (Ph.D. thesis of M.B.) and "Agence National de la Recherche" (reference ANR-18-CE08-014 – MXENECAT project).

REFERENCES

1. Naguib, M.; Kurtoglu, M.; Presser, V.; Lu, J.; Niu, J.; Heon, M.; Hultman, L.; Gogotsi, Y.; Barsoum, M.W. Two-Dimensional Nanocrystals Produced by Exfoliation of Ti_3AlC_2. *Adv. Mater.* **2011**, *23*, 4248–4253.

2. Anasori, B.; Lukatskaya, M.; Gogotsi, Y. 2D Metal Carbides and Nitrides (MXenes) for Energy Storage. *Nat. Rev. Mater.* **2017**, *2*, 16098.

3. Kim, S.-J.; Koh, H.-J.; Ren, C. E.; Kwon, O.; Maleski, K.; Cho, S.-Y.; Anasori, B.; Kim, C.-K.; Choi, Y.-K.; Kim, J. Gogotsi, Y.; Jung, H.-T. Metallic $Ti_3C_2T_x$ MXene Gas Sensors with Ultrahigh Signal-to-Noise Ratio. *ACS Nano* **2018**, *12*, 986–993.

4. Li, Z.; Wu, Y. 2D Early Transition Metal Carbides (MXenes) for Catalysis. *Small* **2019**, *15*. 1804736.

5. Hantanasirisakul, M.; Lipatov, A.; Maleski, K.; Anasori, B.; Salles, P.; Ieosakulrat, C.; Pakawatpanurut, P.; Sinitskii, A.; May, S.J.; Gogotsi, Y. Effects of Synthesis and Processing on Optoelectronic Properties of Titanium Carbonitride MXene. *Chem. Mater.* **2019**, *31*, 2941–2951.

6. Sokol, M.; Natu, V.; Kota, S.; Barsoum, M. W. On the Chemical Diversity of the MAX Phases. *Trends Chem.* **2019**, *1*, 210–223.

7. Hang, J.; Kong, N.; Uzun, S.; Levitt, A.; Seyedin, S.; Lynch, P. A.; Qin, S.; Han, M.; Yang, W.; Liu, J.; Wang, X.; Gogotsi, Y.; Razal, J. M. Scalable Manufacturing of Free-Standing, Strong $Ti_3C_2T_x$ MXene Films with Outstanding Conductivity. *Adv. Mater.* **2020**, *32*, 2001093.

8. Huang, S.; Mochalin, V. N. Hydrolysis of 2D Transition-Metal Carbides (MXenes) in Colloidal Solutions. *Inorg. Chem.* **2019**, *58*, 1958–1966.

9. Lipatov, A.; Lu, H.; Alhabeb, M.; Anasori, B.; Gruverman, A.; Gogotsi, Y.; Sinitskii, A. Elastic Properties of 2D $Ti_3C_2T_x$ MXene Monolayers and Bilayers. *Sci. Adv.* **2018**, *4*, eaat0491.

10. Zhang, C. (J.); McKeon, L.; Kremer, M.P.; Park, S.-H.; Ronan, O.; Seral-Ascaso, A.; Barwich, S.; Coilean, C.O; McEvoy, N.; Nerl, H.C; Anasori, B.; Coleman, J.N.; Gogotsi, Y.; Nicolosi V. Additive-Free MXene Inks and Direct Printing of Micro-Supercapacitors. *Nat. Commun.* **2019**, *10*, 1795.

11. Mariano, M.; Mashtalir, O.; Antonio, F.Q.; Ryu, W.-H.; Deng, B.; Xia, F.; Gogotsi, Y.; Taylor, A.D. Solution-processed Titanium Carbide MXene Films Examined as Highly Transparent Conductors. *Nanoscale* **2016**, *8*, 16371–16378.

12. An, H.; Habib, T.; Shah, S.; Gao, H.; Radovic, M.; Green, M.J.; Lutkenhaus, J.L. Surface-Agnostic Highly Stretchable and Bendable Conductive MXene Multilayers. *Sci. Adv.* ***2018,*** *4*, eaaq0118.

13. Verger, L.; Natu, V.; Carey, M.; Barsoum, M. W. MXenes: An Introduction of Their Synthesis, Select Properties, and Applications. *Trends Chem.* **2019**, *1*, 656–669.

14. Frey, N.C.; Wang, J.; Vega Bellido, G.I.; Anasori. B.; Gogotsi, Y.; Shenoy, V.B. Prediction of Synthesis of 2D Metal Carbides and Nitrides (MXenes) and Their Precursors With Positive and Unlabeled Machine Learning. *ACS Nano*, **2019**, *13*, 3031–3041.

15. Alhabeb, M.; Maleski, K.; Anasori, B.; Lelyukh, P.; Clark, L.; Sin, S.; Gogotsi, Y. Guidelines for Synthesis and Processing of Two-Dimensional Titanium Carbide ($Ti_3C_2T_x$ MXene). *Chem. Mater.* **2017**, *29*, 7633–7644.

16. Persson, P.O.Å.; Rosen, J. Current State of the Art on Tailoring the MXene Composition, Structure, and Surface Chemistry. *Curr. Opin. Solid State Mater. Sci.* **2019**, *23*, 100774.

17. Anayee, M.; Kurra, N.; Alhabeb, M.; Seredych, M.; Hedhili, M.N.; Emwas, A.-H.; Alshareef, H.N.; Anasori, B.; Gogotsi, Y. Role of Acid Mixtures Etching on the Surface Chemistry and Sodium Ion Storage in $Ti_3C_2T_x$ MXene. *Chem. Commun.* **2020**, *56*, 6090–6093.

18. Li, M.; Lu, J.; Luo, K.; Li, Y.; Chang, K.; Chen, K.; Zhou, J.; Rosen, J.; Hultman, L.; Eklund P.; Persson, P.O.A.; Du, S.; Chai, Z.; Huang, Z.; Huang, Q. Element Replacement Approach by Reaction with Lewis Acidic Molten Salts to Synthesize Nanolaminated MAX Phases and MXenes. *J. Am. Chem. Soc.* **2019**, *141*, 4730–4737.

19. Wang, X.; Garnero, C.; Rochard, G.; Magne, D.; Morisset, S.; Hurand, S.; Chartier, P.; Rousseau, J.; Cabioc'h, T.; Coutanceau, C.; Mauchamp, V.; Celerier, S. A New Etching Environment (FeF_3/HCl) for the Synthesis of Two-Dimensional Titanium Carbide MXenes: A Route Towards Selective Reactivity *vs*. Water. *J. Mater. Chem. A.* **2017**, *5*, 22012–22023.

20. Benchakar, M.; Loupias, L.; Garnero, C.; Bilyk, T.; Morais, C.; Canaff, C.; Guignard, N.; Morisset, S.; Pazniak, H.; Hurand, S.; Chartier, P.; Pacaud, J.; Mauchamp, V.; Barsoum, M.W.; Habrioux, A.; Celerier, S. One MAX Phase, Different MXenes: A Guideline to Understand the Crucial Role of Etching Conditions on $Ti_3C_2T_x$ Surface Chemistry. *Appl. Surf. Sci.* **2020**, *560*, 147209.

21. Sang, X.; Xie, Y.; Lin, M.-W.; Alhabeb, M.; Aken, K.L.V.; Gogotsi, Y.; Kent, P.R.C.; Xiao, K.; Unocic, R.R. Atomic Defects in Monolayer Titanium Carbide ($Ti_3C_2T_x$) MXene. *ACS Nano* **2016**, *10*, 9193–9200.

22. Hart, J.L.; Hantanasirisakul, K.; Lang, A.C.; Anasori, B.; Pinto D.; Pivak, Y.; van Omme, T.J.; May, S.J.; Gogotsi, Y.; Taheri, M.L. Control of MXenes' Electronic Properties Through Termination and Intercalation. *Nat. Commun.* **2019**, *10,* 1–10.

23. Seredych, M.; Shuck, C.E.; Pinto, D.; Alhabeb, M.; Precetti, E.; Deysher, G.; Anasori, B.; Kurra, N.; Gogotsi, Y. High-Temperature Behavior and Surface Chemistry of Carbide MXenes Studied by Thermal Analysis. *Chem. Mater.* **2019**, *31*, 3324–3332.

24. Hart, J.; Hantanasirisakul, K.; Lang, A.; Anasori, B.; Gogotsi, Y.; Taheri, M. Direct Correlation of MXene Surface Chemistry and Electronic Properties. *Microsc. Microanal.* **2018,** *24*, 1606–1607.

25. Zhang, P.; Wang, L.; Du, K.; Wang, S.; Huang, Z.; Yuan, L.; Li, Z.; Wang, H.; Zheng, L.; Chai, Z.; Shi, W. Effective Removal of U(VI) and Eu(III) by Carboxyl Functionalized MXene Nanosheets. *J. Hazard. Mater.* **2020**, *396*, 122731.

26. Chen, C.; Boota, M.; Urbankowski, P.; Anasori, B.; Miao, L.; Jiang, J.; Gogotsi, Y. Effect of Glycine Functionalization of 2D Titanium Carbide (MXene) on Charge Storage. *J. Mater. Chem. A* **2018**, *6*, 4617–4622.

27. Riazi, H.; Anayee, M.; Hantanasirisakul, K.; Shamsabadi, A.A.; Anasori, B.; Gogotsi, Y.; Soroush, M. Surface Modification of a MXene by an Aminosilane Coupling Agent. *Adv. Mater. Interfaces* **2020**, *7*, 1902008.

28. Huang, Z.; Liu, B.; Liu, J. Mn^{2+}-Assisted DNA Oligonucleotide Adsorption on Ti_2C MXene Nanosheets. *Langmuir*, **2019**, *35*, 9858–9866.

29. Jiang, X.; Kuklin, A.V.; Baev, A.; Ge, Y.; Ågren, H.; Zhang, H.; Prasad, P.N. Two-Dimensional MXenes: From Morphological to Optical, Electric, and Magnetic Properties and Applications. *Phys. Rep.* **2020**, *848*, 1–58.

30. Lukatskaya, M.R.; Mashtalir, O.; Ren, C.E.; Dall'Agnese, Y.; Rozier, P.; Taberna, P.L.; Naguib, M.; Simon, P.; Barsoum, M.W.; Gogotsi, Y. Cation Intercalation and High Volumetric Capacitance of Two-Dimensional Titanium Carbide. *Science*, **2013**, *341*, 1502–1505.

31. Al-Temimy, A.; Anasori, B.; Mazzio, K.A.; Kronast, F.; Seredych, M.; Kurra, N.; Mawass, M.-A.; Raoux, S.; Gogotsi, Y.; Petit, T. Enhancement of Ti_3C_2 MXene Pseudocapacitance After Urea Intercalation Studied by Soft X-Ray Absorption Spectroscopy. *J. Phys. Chem. C*, **2020**, *124*, *9*, 5079–5086.

32. Li, J.; Yuan, X.; Lin, C.; Yang, Y.; Xu, L.; Du, X.; Xie, J.; Lin, J.; Sun, J. Achieving High Pseudocapacitance of 2D Titanium Carbide (MXene) by Cation Intercalation and Surface Modification. *Adv. Energy Mater.* **2017**, *7*, 1602725.

33. Ghidiu, M.; Halim, J.; Kota S.; Bish, D.; Gogotsi Y.; Barsoum, M.W. Ion-Exchange and Cation Solvation Reactions in Ti_3C_2 MXene. *Chem. Mater.* **2016**, *28*, 3507–3514.

34. Koh, H.-J.; Kim, S.J.; Maleski, K.; Cho, S.-Y.; Kim, Y.-J.; Ahn, C.W.; Gogotsi, Y.; Jung, H.-T. Enhanced Selectivity of MXene Gas Sensors Through Metal Ion Intercalation: *in Situ* X-Ray Diffraction Study. *ACS Sens.* **2019**, *4*, 1365–1372.

35. Gao, Q.; Come, J.; Naguib, M.; Jesse, S.; Gogotsi, Y.; Balke, N. Synergetic Effects of K^+ and Mg^{2+} Ion Intercalation on the Electrochemical and Actuation Properties of the Two-Dimensional Ti_3C_2 MXene. *Faraday Discuss.* **2017**, *199*, 393–403.

36. Mashtalir, O.; Lukatskaya, M.R.; Kolesnikov, A.I.; Raymundo-Pinero, E.; Naguib, M.; Barsoum M.W.; Gogotsi, Y. Effect of Hydrazine Intercalation on Structure and Capacitance of 2D Titanium Carbide (MXene). *Nanoscale* **2016**, *8*, 9128–9133.

37. Tao, Q.; Dahlqvist, M.; Lu, J.; Kota, S.; Meshkian, R.; Halim, J.; Palisaitis, J.; Hultman, L.; Barsoum, M.W.; Persson, P.O.Å.; Rosen, J. Two-Dimensional $Mo_{1.33}C$ MXene with Divacancy Ordering Prepared from Parent 3D Laminate with In-Plane Chemical Ordering. *Nat. Commun*. **2017**, *8*, 14949.

38. Halim, J.; Palisaitis, J.; Lu, J.; Thörnberg, J.; Moon, E.J.; Precner, M.; Eklund, P.; Persson, P.O.Å.; Barsoum, M.W.; Rosen, J. Synthesis of Two-Dimensional $Nb_{1.33}C$ (MXene) with Randomly Distributed Vacancies by Etching of the Quaternary Solid Solution $(Nb_{2/3}Sc_{1/3})_2AlC$ MAX Phase. *ACS Appl. Nano Mater.*, **2018**, *1*, 2455–2460.

39. Yang, L.; Dall'Agnese, C.; Dall'Agnese, Y.; Chen, G.; Gao, Y.; Sanehira, Y.; Jena, A. K.; Wang, X.-F.; Gogotsi, Y.; Miyasaka, T. Surface-Modified Metallic $Ti_3C_2T_x$ MXene as Electron Transport Layer for Planar Heterojunction Perovskite Solar Cells. *Adv. Funct. Mater.* **2019**, *29*, 1905694.

40. Hu, T.; Sun, W.; Hu, M.; Cheng, R.; Wang, X. Atomic Repartition in MXenes by Electron Probes. *Chem. Mater.* **2019**, *31*, 4385–4391.

41. Romer, F.M.; Wiedwald, U.; Strusch, T.; Halim, J.; Mayerberger, E.; Barsoum, M.W.; Farle, M. Controlling the Conductivity of Ti_3C_2 MXenes by Inductively Coupled Oxygen and Hydrogen Plasma Treatment and Humidity. *RSC Adv.* **2017**, *7*, 13097–13103.

42. Williams, J.S. Ion Implantation of Semiconductors. *Mat. Sci. Eng. A* **1998**, *253*, 8–15.

43. Fávaro de Oliveira, F.; Antonov, D.; Wang, Y.; Neumann, P.; Momenzadeh, S.A.; Häußermann, T.; Pasquarelli. A.; Denisenko, A.; Wrachtrup, J. Tailoring Spin Defects in Diamond by Lattice Charging. *Nat. Commun.* **2017**, *8*, 15409.

44. Bradac, C.; Gao, W.; Forneris, J.; Trusheim, M.E.; Aharonovich, I. Quantum Nanophotonics with Group IV Defects in Diamond. *Nat. Commun.* **2019**, *10*, 5625.

45. Li, Z.; Chen, F. Ion Beam Modification of Two-Dimensional Materials: Characterization, Properties, and Applications. *Appl. Phys. Rev.* **2017**, *4*, 011103.

46. Willke, P.; Amani, J.A.; Sinterhauf, A.; Thakur, S.; Kotzott, T.; Druga, T.; Weikert, S.; Maiti, K.; Hofsass, H.; Wenderoth, M. Doping of Graphene by Low-Energy Ion Beam Implantation: Structural, Electronic, and Transport Properties. *Nano Lett.* **2015**, *15*, 5110–5115.

47. Xu, Y.; Zhang, K.; Brusewitz, C.; Wu, X.; Hofsass, H.C. Investigation of the Effect of Low Energy Ion Beam Irradiation on Mono-Layer Graphene. *AIP Advances* **2013**, *3*, 072120.

48. Willke, P.; Amani, J.A.; Thakur, S.; Weikert, S.; Druga, T.; Maiti, K.; Hofsass, H.; Wenderoth, M. Short-Range Ordering of Ion-Implanted Nitrogen Atoms in SiC-Graphene. *Appl. Phys. Lett.* **2014**, *105*, 111605.

49. Wang, Q.; Shao, Y.; Ge, D.; Yang, Q.; Ren, N. Surface Modification of Multilayer Graphene Using Ga Ion Irradiation. *J. Appl. Phys.* **2015**, *117*, 165303.

50. Ahlberg, P.; Johansson, F.O.L.; Zhang, Z.-B.; Jansson, U.; Zhang, S.-L.; Lindblad, A.; Nyberg, T. Defect Formation in Graphene During Low-Energy Ion Bombardment. *APL Materials* **2016**, *4*, 046104.

51. Ochedowski, O.; Marinov, K.; Wilbs, G.; Keller, G.; Scheuschner, N.; Severin, D.; Bender, M.; Maultzsch, J.; Tegude, F.J.; Schleberger, M. Radiation Hardness of Graphene and MoS_2 Field Effect Devices Against Swift Heavy Ion Irradiation. *J. Appl. Phys.* **2013**, *113*, 214306.

52. Ochedowski, O.; Bukowska, H.; Soler, V.M.F.; Brokers, L.; Ban-d'Etat, B.; Lebius, H.; Schleberger, M. Folding Two Dimensional Crystals by Swift Heavy Ion Irradiation. *Nucl. Instum. Meth. B* **2014**, *340*, 39–43.

53. Shlimak, I.; Zion, E.; Butenko, A.V.; Wolfson, L.; Richter, V.; Kaganovskii, Yu.; Sharoni, A.; Haran, A.; Naveh, D.; Kogan, E.; Kaveh, M. Hopping Magnetoresistance in Ion Irradiated Monolayer Graphene. *Physica E Low Dimens. Syst. Nanostruct.* **2016**, *76*, 158–163.

54. Tsukagoshi, A.; Honda, C.-I.; Osugi, R.; Okada, H.; Niibe, M.; Terasawa, M.; Hirase, R.; Izumi, H.; Yoshioka, H.; Niwase, K.; Taguchi, E.; Lee, K.-Y.; Oura, M. Spectroscopic Characterization of Ion-Irradiated Multi-Layer Graphenes. *Nucl. Instum. Meth. B* **2013**, *315*, 64–67.

55. Fox, S.D.; Zhou, Y.; Maguire, P.; O'Neill, A.; O'Coileain, C.; Gatensby, R.; Glushenkov, A.M.; Tao, T.; Duesberg, G.S.; Shvets, I.V.; Abid, M.; Abid, M.; Wu, H.-C.; Chen, Y.; Coleman, J.N.; Donegan, J.F.; Zhang, H. Nanopatterning and Electrical Tuning of MoS_2 Layers with a Subnanometer Helium Ion Beam. *Nano Lett.* **2015**, *15*, 5307–5313.

56. Stanford, M.; Pudasaini, P.; Belianinov, A.; Cross, N.; Noh, J.H.; Koehler, M.R.; Mandrus, D.G.; Duscher, G.; Rondinone, A.J.; Ivanov, I.N.; Ward, T.Z.; Rack, P.D. Focused Helium-Ion Beam Irradiation Effects on Electrical Transport Properties of Few-Layer WSe_2: Enabling Nanoscale Direct Write Homo-Junctions. *Sci. Rep.* **2016**, *6*, 27276.

57. He, S.M.; Huang, C.C.; Liou, J.W.; Woon, W.Y.; Su, C.Y. Spectroscopic and Electrical Characterizations of Low-Damage Phosphorous-Doped Graphene *via* Ion Implantation. *ACS Appl. Mater. Interfaces* **2019**, *11*, 47289–47298.

58. Anasori, B.; Gogotsi, Y. 2D Metal Carbides and Nitrides (MXenes); Springer, Cham, Switzerland, 2019; pp 291–300.

59. Ghidiu, M.; Lukatskaya, M. R.; Zhao, M.-Q.; Gogotsi, Y.; Barsoum, M. W. Conductive Two-Dimensional Titanium Carbide 'Clay' with High Volumetric Capacitance. *Nature* **2014**, *516*, 78–81.

60. Momma, F.; Izumi, F. Vesta 3 for Three-Dimensional Visualization of Crystal, Volumetric and Morphology Data. *J. Appl. Crystallogr.* **2011**, *44*, 1272–1276.

61. Halim, J.; Cook, K. M.; Naguib, M.; Eklund, P.; Gogotsi, Y.; Rosen, J.; Barsoum, M. W. X-Ray Photoelectron Spectroscopy of Select Multi-Layered Transition Metal Carbides (MXenes). *Appl. Surf. Sci.* **2016**, *362*, 406–417.

62. Wang, X.; Shen, X.; Yu, R.; Chen, L. Atomic-Scale Recognition of Surface Structure and Intercalation Mechanism of Ti_3C_2X. *J. Am. Chem. Soc.* **2015**, *137*, 2715–2721.

63. Cheng, Z.; Abuzaid, H.; Yu, Y.; Zhang, F.; Li, Y.; Noyce, S.G.; Williams, N.X.; Lin, Y.-C.; Doherty, J.L.; Tao, C.; Cao, L.; Franklin, A.D. Convergent Ion Beam Alteration of 2D Materials and Metal-2D Interfaces. *2D Mater.* **2019**, *6*, 034005.

64. Xu, K.; Zhao, Y.; Lin, Z.; Long, Y.; Wang, Y.; Chan, M.; Chai, Y. Doping of Two-Dimensional MoS_2 by High Energy Ion Implantation. *Semicond. Sci. Technol.* **2017**, *32*, 124002.

65. Busby, Y.; Franquet, A.; Spampinato, V.; Casula, G.; Bonfiglio, A.; Cosseddu, P.; Pireaux, J.-J.; Houssiau, L. Combined AFM and ToF-SIMS Analyses for the Study of Filaments in Organic Resistive Switching Memories. *Proc. SPIE 10738, Organic and Hybrid Sensors and Bioelectronics XI*, San Diego, California, **2018**, 1073814.

66. Noël, C.; Pescetelli, S.; Agresti, A.; Franquet, A.; Spampinato, V.; Felten, A.; Di Carlo, A.; Houssiau, L.; Busby, Y. Hybrid Perovskites Depth Profiling with Variable-Size Argon Clusters and Monatomic Ions Beams. *Materials* **2019**, *12*, 726.

67. Madauß, L.; Zegkinoglou, I.; Muiños, H.V.; Choi, Y.-W.; Kunze, S.; Zhao, M.-Q.; Naylor, C.H.; Ernst, P.; Pollmann, E.; Ochedowski, O.; Lebius, H.; Benyagou, A.; Ban-d'Etat, B.; Johnson, A.T.C.; Djurabekova, F.; Cuenya, B.R.; Schleberger, M. Highly Active Single-Layer MoS_2 Catalysts Synthesized by Swift Heavy Ion Irradiation, *Nanoscale* **2018**, *10*, 22908–22916.

68. Ghorbani-Asl, M.; Kretschmer, S.; Spearot, D.E.; Krasheninnikov, A.V. Two-Dimensional MoS_2 Under Ion Irradiation: From Controlled Defect Production to Electronic Structure Engineering. *2D Mater*. **2014**, *4*, 025078.

69. Magnuson, M.; Halim, J.; Näslund, L.-A. Chemical Bonding in Carbide MXene Nanosheets. *J. Electron. Spectrosc.* **2018**, *224*, 27–32.

70. Bugnet, M.; Mauchamp, V.; Eklund, P.; Jaouen, M.; Cabioc'h, T. Contribution of Core-Loss Fine Structures to the Characterization of Ion Irradiation Damages in the Nanolaminated Ceramic Ti_3AlC_2. *Acta Mater*. **2013**, *61*, 7348–7363.

71. Mironov, B.E.; Freeman, H.M.; Brown, A.P.; Hage, F.S.; Scott, A.J.; Westwood, A.V.K.; Da Costa, J.-P.; Weisbecker, P.; Brydson, R.M.D. Electron Irradiation of Nuclear Graphite Studied by Transmission Electron Microscopy and Electron Energy Loss Spectroscopy. *Carbon* **2015**, *83*, 106–117.

72. Abdallah, I.; Dupressoire, C.; Laffont, L.; Monceau, D.; Put, A.V. STEM-EELS Identification of TiO_xN_Y, TiN, Ti_2N and O, N Dissolution in the Ti264S Alloy Oxidized in Synthetic Air at 650 ^oC. *Corros. Sci.* **2019**, *153*, 191–199.

73. Magne, D.; Mauchamp, V.; Célérier, S.; Chartier, P.; Cabioc'h, T. Site-Projected Electronic Structure of Two-Dimensional Ti_3C_2 MXene: The Role of the Surface Functionalization Groups. *Phys. Chem. Chem. Phys.* **2016**, *18*, 30946–30953.

74. Mkhoyan, K.A.; Contryman, A.W.; Silcox, J.; Stewart, D.A.; Eda, G.; Mattevi, C.; Miller, S.; Chhowalla, M. Atomic and Electronic Structure of Graphene-Oxide. *Nano Lett*. **2009**, *9*, 1058–1063.

75. Xia, F.; Lai, J.; Yu, R.; Sang, X.; Luo, J.; Li, Y.; Wu, J. Ambient Oxidation of Ti_3C_2 MXene Initialized by Atomic Defects. *Nanoscale*, **2019**, *11*, 23330–23337.

76. Ziegler, J.; Ziegler, M.; Biersack, J. SRIM – The Stopping and Range of Ions in Matter. *Nucl. Instrum. Meth. B* **2010**, *268*, 1818–1823.

For Table of Contents Only